Regular Article
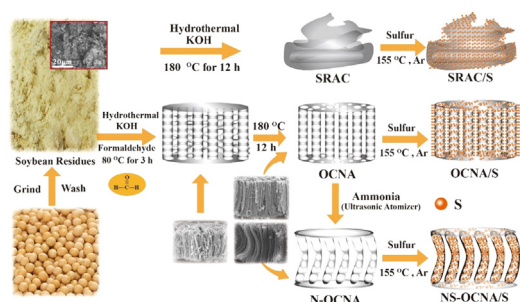
Nitrogen/sulfur co-doped ordered carbon nanoarrays for superior sulfur hosts in lithium-sulfur batteries

Xiaoyu Wen, Xiaowei Lu, Kaixiong Xiang, Li Xiao, Haiyang Liao, Wenhao Chen, Wei Zhou, Han Chen *

School of Metallurgy and Materials Engineering, Hunan University of Technology, Zhuzhou, Hunan 412007, PR China

GRAPHICAL ABSTRACT

ARTICLE INFO

ABSTRACT

A universal and low-cost biomass waste, soybean residue, that was derived from a soybean product processing plant, was used to fabricate nitrogen/sulfur co-doped, ordered carbon nanoarrays (NS-OCNA/S). The effects of nitrogen and sulfur co-doping and the addition of formaldehyde on the structure and properties of these novel materials were investigated using X-ray diffraction (XRD), Raman spectrometry, scanning electron microscopy (SEM) techniques and galvanostatic charge/discharge tests. With high levels of sulfur doping, the nitrogen/sulfur co-doped ordered carbon nanoarrays (NS-OCNA/S) were found to possess hierarchical pores and a high pore volume. The NS-OCNA/S exhibited good electrical conductivity, excellent discharge capacity and cycling performance. When the NS-OCNA/S was used in Li-S batteries it was found that the charge capacity of the cell decayed from 914 to 739 mAh g^{-1}, with a capacity retention 81% over 600 cycles at 2 C. This successful research effort has identified new, high-performance materials derived from bio-resources for use in Li-S batteries.

© 2019 Elsevier Inc. All rights reserved.

1. Introduction

Rechargeable lithium-ion batteries (LIBs) have been commercially applied in electric vehicles (EVs) and hybrid electric vehicles (HEVs). To meet the requirements of EVs and HEVs, lithium-sulfur (Li-S) batteries are considered to the preferred candidate for the next generation LIBs due to their ultrahigh capacity (1675 mAh g^{-1}), which is five times greater than the commercial

LIBs. Moreover, the sulfur cathode is the most competitive among various LIBs cathodes due to its natural abundance, convenience and safety [1,2]. Nevertheless, the poor conductivities of sulfur and its discharge products Li_2S_2/Li_2S [3,4], the drastic volume change (about 80%) of sulfur during charge/discharge process and the serious shuttling effect caused by the dissolution of polysulfides in the electrolyte in Li-S batteries result in low utilization, bad cycle stability and poor coulombic efficiency, which restrict the commercialization of Li-S batteries [5-8].

To resolve these short comings, modification of the sulfur cathode has been extensively explored by both domestic and foreign

researchers [9-11]. These studies have reported that porous carbon with a specified structure combined with elemental sulfur can be a common and effective approach for fabricating effective carbon-sulfur composite materials. Volumetric expansion of the carbon-sulfur composite cathodes can be relieved by the flexibility of the porous carbon, thus preventing significant structural changes in the electrode. In addition, the high pore volume of porous carbon offers higher sulfur loading and can trap lithium polysulfides through physical adsorption, which can help to inhibit the polysulfide shuttle effect [12-17]. MnO_2 nanosheets were grown on both sides of the N-doped hollow porous carbon for advanced Li-S batteries. These composite materials exhibited an initial discharge capacity of 1249 mAh g^{-1} at 0.5 C [18]. Metal-organic frameworks (MOFs) have been widely development in recent years, because of their special structural features including tunable porosity and a large internal surface area. The thermal transformation of MOFs into carbon nanomaterials can successfully maintain the large surface area and porosity of MOFs, which can result in porous carbons modified with a uniform metallic species [19]. MOF-derived porous carbons and carbon nanotubes were synthesized in this reported effort and used in lithium-sulfur batteries. This material was found to exhibited outstanding cycle stability, a remarkable high-rate response up to 10 C [20].

However, the synthesis process used to produce these carbon materials has serious faults, such as use of strong acid, strong alkali and strong oxidants that are environmentally objectionable and high cost that limits their energy storage application. Activated carbons exhibit good electrochemical properties, renewability, environmental friendliness and low-cost, and they are prepared from biomass and carbonaceous mineral by a facile carbonization procedure [21-24]. Recently, natural biomass-derived porous carbons have exhibited potential application in Li-S batteries. These materials were derived from various sources including, pomelo peel [25,26], fish scale [27], bamboo [28], corncob [29], luffa sponge [30,31], eggshell membrane [32] and leaf [33], which are safe, convenient, and naturally abundant. A hierarchical porous carbon/sulfur composites was produced using lotus seedpod shells for use in a lithium-sulfur battery. It exhibited a remarkable initial capacity (1138 mAh g^{-1} at 0.5 C), low capacity decay of 0.16% per cycle and high coulombic efficiency of about 97% [34]. Coconut shells were used to synthesize porous carbon materials, which exhibited great discharge capacities of 1500 mA h g^{-1} at 2.0 C and a high reversible capacity of 517 mA h g^{-1} at 2.0 C over 400 cycles [35].

Furthermore, porous carbon modified with heteroatom doping of B, N, P and S has been a predominant strategy for adjusting and controlling the surface chemistry and the electronic properties of activated carbons and has been extensively investigated in the energy materials field [36,37]. In the Li-S batteries, element doping can effectively increase the amount of sulfur in the carbon material and inhibit the polysulfide shuttle effect through strong chemical bonding between the resident heteroatoms and sulfur atoms [38-40]. For instance, a novel strategy was reported for preparing a sulfur cathode by introducing nitrogen doped mesoporous carbon nanofibers, which improved the electronic conductivity of the nitrogen doped carbon. This material exhibited an excellent rate capability and cycling stability [41].

Soybean residues are the main byproduct of soybean product processing and are usually used as fodder for livestock or discarded as waste. These residues are primarily composed of cellulose, hemicellulose and lignin. Porous carbon derived from soybean residues have been employed to produce the activated carbon used in lithium-ion batteries, supercapacitors and in the lithium sulfur battery [42-46]. In particular, we have reported on a bean-dreg-derived carbon modified by graphitization and activation treatments for use in LIB anodes. This material was found to exhibit enhanced electrochemical performance due to its appropriate graphitization and physical properties [45]. A honeycomb structured-like N and O element co-doped porous carbon was fabricated via KOH activation using bean dreg as the precursor to encapsulate sulfur [47]. The reported composite exhibited outstanding initial capacity (1185 mAh g^{-1} at 0.2 C) with a high sulfur content (64.5 wt%).

Herein, we report on a novel approach to prepare ordered carbon nanoarrays using soybean residues as the precursor. Formaldehyde was the structure-inducing agent in this low-temperature hydrothermal process and it played a vital role in the formation of ordered carbon nanoarrays (OCNA). Moreover, nitrogen doping is crucial to regulate the microstructure, pore structure and porosity of the carbon. The synthesized nitrogen-doped OCNA (N-OCNA) possessed hierarchical pores, a large surface area, suitable pore size distribution, and an appropriate nitrogen content. These special physical properties endowed the N-OCNA with fast ion transportation, high sulfur loading and strong chemical adsorption for immobilizing lithium polysulfides. Furthermore, sulfur was loaded and doped simultaneously during the sulfur loading processes (NS-OCNA/S). Hence, the NS-OCNA/S composite behaved well in terms of reversible capacity, cycling and rate performance.

2. Experimental

2.1. Preparation of carbons

The fresh soybean residues (SR) collected from breakfast shop were extensively cleaned with deionized water and hydrochloric acid to eliminate redundant impurities. 2 g of soybean residues and 8 g potassium hydroxide were placed into a Teflon-lined stainless autoclave with 60 mL of deionized water and 20 mL formaldehyde solution (36.5%). The autoclave was then placed into an electric oven at 80 °C for 3 h and at 180 °C for 12 h. The resulting product was, filtrated, and washed with deionized water. Next, the sample was calcined at 800 °C under argon flow in the tube furnace for 1 h. The carbon product was cleaned and labeled OCNA. As a control, KOH activated carbons (denoted as SRAC) were also produced using the previously mentioned procedure without the formaldehyde solution.

The nitrogen doping process was conducted consisted of the following steps. First, the prepared OCNA sample was placed into a quartz boat in the tube furnace. A bottle containing 30 mL ammonia with a concentration of 25% ∼ 28% was placed into an ultrasonic atomizer. Second, the tube furnace was heated to 800 °C, and then the ammonia output from ultrasonic atomizer fed into the 800 °C tube furnace for 2 h. The resulting N-doped carbon sample was donated as N-OCNA.

To prepare the SRAC/S, OCNA/S composites, 0.15 g SRAC and OCNA were each individually dispersed into 400 mL DI water, and 4.9636 g $Na_2S_2O_3$ was added to these solutions. After vigorous stirring for 1 h, 4 mL hydrochloric acid was slowly added to the solutions and stirred for a day. Finally, the resulting samples were placed into sealed bottles and heated at 155 °C for 12 h and then at 250 °C for 1 h. When cooled to room temperature, the SRAC/S and OCNA/S composites were obtained. More importantly, sulfur was also loaded and doped using the same above processes to produce NS-OCNA/S composites using N-OCNA as the starting materials.

2.2. Materials characterization

X-ray diffraction patterns (XRD) of the samples were obtained using on a Rigaku Ultima IV instrument. Raman spectra of the experimental materials were acquired using a Invia Qontor with a laser wavelength of 514 nm. The microscopic features of samples were characterized using scanning electron microscopy (SEM)

(JSM-7001F, JEOL, Tokyo, Japan) and transmission electron microscopy (TEM) (SU7000, JEOL, Tokyo, Japan). The elemental mapping analysis of the samples was conducted using an energy dispersive spectrometer (EDS). Sulfur loading in the composites was measured using a thermogravimetric analyzer (TGA, SDTQ600) with a heating rate of 5 °C min^{-1} from room temperature to 800 °C. Nitrogen adsorption-desorption isotherms of the samples were obtained using a 3H-2000PMC via the Brunauer-Emmett-Teller (BET) method. X-ray photoelectron spectroscopy (XPS) analysis was conducted on the samples using a ESCALAB 250Xi with an Al Kα achromatic x-ray source operating at 12 kV.

2.3. Evaluation of electrochemical properties

Electrodes were prepared using the experimental materials for lithium-sulfur batteries by mixing the carbons with acetylene black, and polyvinylidene fluoride (PVDF) in an 8:1:1 ratio, together with N-methylpyrrolidone. The resulting slurries were coated onto individual 25 μm thin Al foils and dried at 60 °C overnight. These foils were used as the positive electrode in CR2025 coin-type cells that were assembled in a glove box. The mass loading of active material in the electrodes was about 2.5 mg cm^{-2}, the three C/S composite electrodes had various sulfur loadings, ranged from 47 to 85%, corresponding to the area sulfur content of 1.18–2.14 mg cm^{-2}. The electrolyte used was 1 mol L^{-1} lithium bis(tri fluoromethanesulfonyl)imide (LiTFSI) salt in a solvent mixture of dimethoxyethane (DME) and 1,3-dioxolane (DOL) (V/V = 1:1) with 3 wt% LiNO$_3$. The evaluation of electrochemical properties was conducted using a Neware BTS-5V10 mA in a voltage range between 1.7 and 2.8 V (~vs. Li/Li$^+$). Electrochemical impedance spectroscopy (EIS) analysis was conducted on the coin cells at open circuit over a frequency region from 100 kHz to 10 mHz by applying an AC signal of 5 mV in amplitude throughout the test.

3. Results and discussion

The carbon composites synthesis procedure for preparing the SRAC/S, OCNA/S and NS-OCNA/S is illustrated in Fig. 1. The SRAC was synthesized by hydrothermal treatment with KOH. Then, the SRAC was treated with Na$_2$S$_2$O$_3$ as the sulfur sources to prepare the SRAC/S composites, and as such Fig. 1 shows that sulfur particles covered the SRAC surface. The fresh soybean residues were treated with formaldehyde as the structural inducing agent and with KOH as the chemical activation agent to produce the OCNA powders. KOH activation can produce abundant porosity in the carbon, because the KOH erodes the carbon. The addition of the formaldehyde promotes the condensation reaction between the aldehyde groups of formaldehyde and hydroxyl groups of the soybeans during the low temperature hydrothermal process, which ensures the formation of ordered carbon nanoarrays. Moreover, it is worthwhile mentioning that formaldehyde can effectively prevent lignin condensation during the hydrothermal process through the reaction between the aldehydes and hydroxyl groups to form a stable structure. In addition, formaldehyde can also produce active sites that inactivate lignin condensation, which and improves the morphologies of the biomass carbon by taking advantage of good ductility of lignin [48].

The FTIR spectra of the soybean powders exhibited the characteristic peaks at 3744, 1513, 1080 and 665 cm^{-1}, which were attributed respectively to the —OH, C—C, C—O—C and C—H groups, while the C=O absorbance bond was present at 2364 and 1694 cm^{-1} (Fig. S1). Therefore, the added formaldehydes appeared to facilitate the orderly assembly of ordered nanoarrays (OCNA). The OCNA was then N-doped with ammonia using the ultrasonic atomizer to obtain the N-OCNA. During this process, the pore structure and pore distribution of the N-OCNA were regulated by the presence of the water vapor at high temperature. The sulfur particles were loaded into the OCNA and N-OCNA using Na$_2$S$_2$O$_3$ as the sulfur source. The cavities and pores were predominantly occupied by sulfur particles to produce the OCNA/S composites, and the sulfur particles were also coated on the carbon nanorods due to difficulty of the infiltration of the sulfur particles into the dense carbon. However, sulfur particles were easily loaded into the prepared N-OCNA and distributed uniformly in the N-OCNA to produce the N-OCNA/S composites. Moreover, sulfur particles appeared to completely penetrate the N-doping carbons, since no
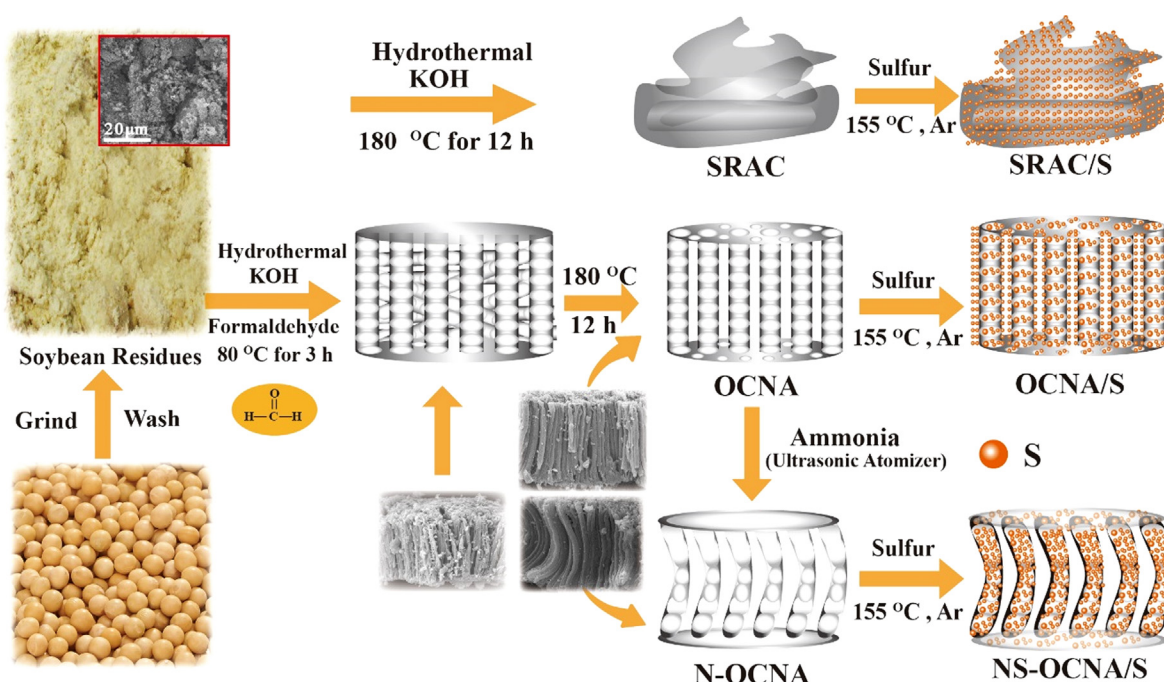

Fig. 1. Schematic diagram of the synthesis procedure for DOC/S, FOCA/S, NSFOCA/S.

sulfur was found on the surface of N-doping carbon nanorods due to the difficulty of the infiltration of sulfur particles in the loose, porous and homogeneous carbon. Simultaneously, sulfur was successfully doped into the N-OCNA to produce the NS-OCNA/S composites during the sulfur loading process. N/S co-doping of the ordered composite materials greatly improved the chemisorption of sulfur particles in the NS-OCNA/S composite.

The SEM images for the SRAC, OCNA and N-OCNA are shown in Fig. 2a and g and Fig. S2. The SEM images for the SRAC show rambling, short, carbon rods and randomly stacked carbon debris and particles (Fig. S2c and d). The SEM images for the OCNA show that the length and diameter of the uniform carbon rods were about 32 μm and 3.5 μm, respectively (Fig. S3a). Additionally, the uniform carbon rods appeared to be orderly, parallel and regularly arranged into ordered carbon nanoarrays by thin carbon layers on the top and bottom. Furthermore, a substantial number of uniform pores with a diameter of 1.7 μm can be distinguished from the circles at the side and top of the Figure (Fig. 2a and Fig. S3b). The preserved hollows originated from the structural pores of the soybean residues. After nitrogen doping, N-OCNA displayed significant changes compared to OCNA (Fig. 2g and Fig. S3c,d). In the N-OCNA, the carbon rods exhibited slight bends due to the decrease in volume and no the hollows were present in the carbon rods.

Also, puffy sponge-like carbon layers were observed on the top and bottom. These evident changes were attributed to the mutual effects of the nitrogen doping and re-activation of water vapor on the structure of carbon materials.

Fig. 2b, h and Fig. S4 show the SEM images of SRAC/S, OCNA/S and NS-OCNA/S. It can be seen from these figures that the morphologies of the SRAC and OCNA exhibited discrete obvious changes after the sulfur loading. Many small particles can be seen on the SRAC/S materials, which were due to the coating of sulfur particles on the SRAC surface (Fig. S4a and b). The previously evident pores on the sides, tops and bottoms of the OCNA material had completely disappeared, and inhomogeneous, thin carbon layers were substituted by a uniform layer of sulfur particles, suggesting that the pores in the OCNA/S were filled with sulfur particles (Fig. 2b and Fig. S4c). However, it appeared that negligible changes had occurred on the surface of NS-OCNA/S after the sulfur loading (Fig. 2h), which demonstrated that the sulfur particles were well-dispersed in the NS-OCNA/S materials. A few particles appeared to adhere to the surface of the NS-OCNA/S composites. Most of broken pores were stuffed with sulfur particles, which can be seen from the top of carbon nanorods (Fig. S4e). In particular, there was a cluster of sulfur on the top pore, indicating the influx of sulfur particles into the pores (Fig. S4f).
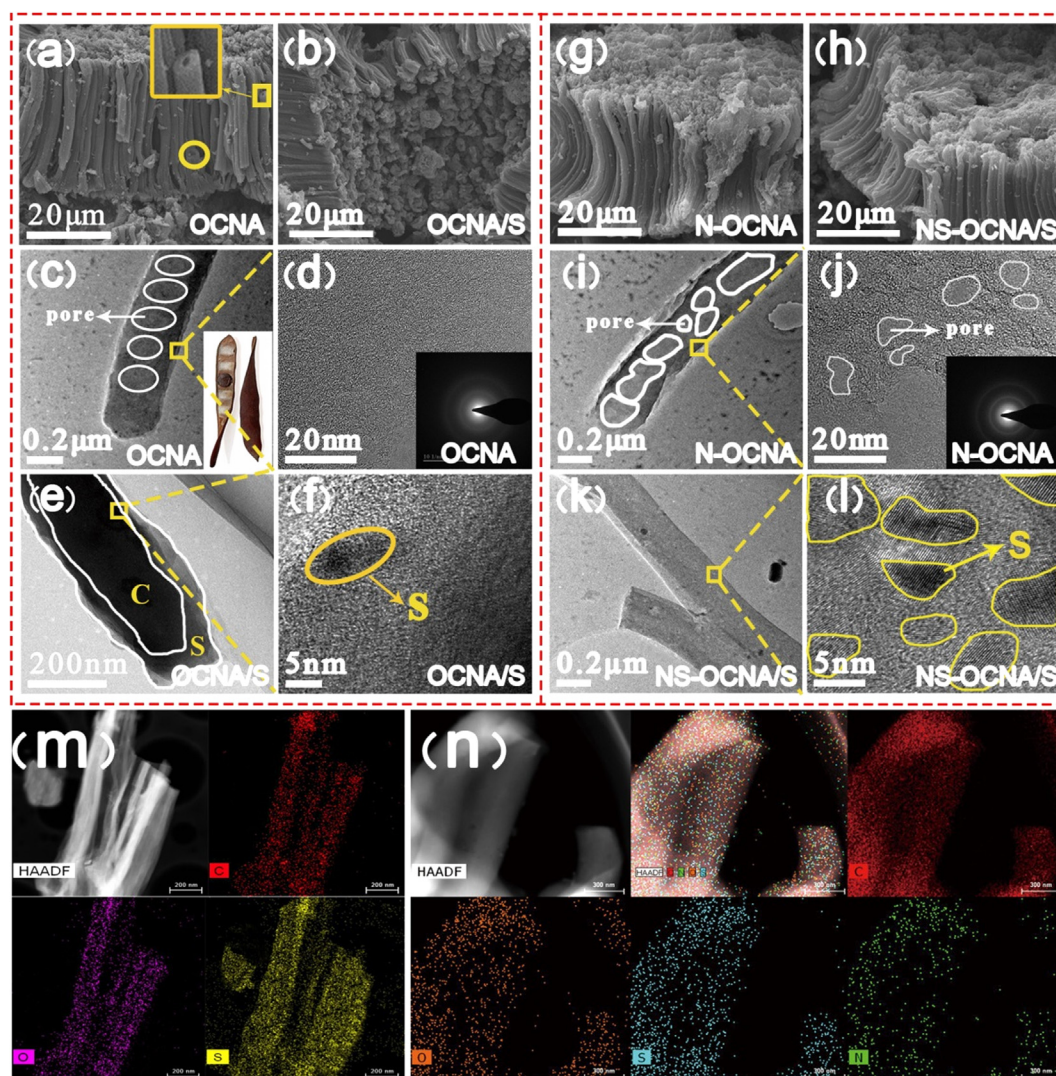
Fig. 2. SEM images of (a) OCNA, (g) N-OCNA, (b) OCNA/S, (h) NS-OCNA/S; TEM images of (c, d) OCNA and (e, f) OCNA/S; and TEM images of (i, j) N-OCNA and (k, l) NS-OCNA/S. HAADF-STEM and EDS elemental mappings images of OCNA/S (m) and NS-OCNA/S (n).

As shown in Fig. S4g–i, the elemental distributions in the SRAC/S, OCNA/S and NS-OCNA/S were determined using low-magnified SEM observations with elemental mapping. The sulfur-rich regions of the three composites completely overlapped the carbon-rich regions, demonstrating that sulfur particles had infiltrated into the carbon matrix. Notably, as shown in Fig. S4i, the presence of nitrogen and the perfect overlap of its distribution with that of carbon confirmed that nitrogen was successfully doped into carbon framework. However, the degree of sulfur doping was difficult to determine due to the high sulfur loading of the composites. In addition, Fig. S5 and Table S1 show the energy dispersive spectroscopy (EDS) analysis results that provides the elemental composition of the prepared composites, and it can be seen that the nitrogen content of the NS-OCNA/S composites was 5.28 wt%.

The TEM images and the EDS elemental mapping analysis of the experimental materials (Fig. 2c-n and Fig. S6) revealed their microstructure and chemical composition before and after sulfur loading. The TEM images of SRAC (Fig. S6a and b) revealed a non-porous compact carbon texture. OCNA and N-OCNA appeared to have uniform nanorods about 250 nm in diameter, but their interior structures exhibited significant differences. The regular macropores in the materials of about 180 nm in size were arranged in good order (Fig. 2c) and the carbon walls were evidently compact (Fig. 2d). Therefore, OCNA had a more pod-like structure after removal of the bean material as shown in Fig. 2c. These pores in the product may be attributed to the original macropores provided by the intrinsic pores of the soybean precursor that were enlarged by the KOH activation. However, the regular pore structure appeared to have been broken and was obviously changed to irregular pores ranging in size from 20 to 150 nm (Fig. 2i), and the carbon walls have numerous micropores (Fig. 2j). The varieties of macropores and the formation of micropores and mesopores resulted from the nitrogen doping, activation via water vapor and erosion by high temperature ammonia. The hierarchical porous structures of the OCNA and N-OCNA favored the loading and stabilizing of a great deal of sulfur. Furthermore, these hierarchical porous structures accommodated the impregnation of the electrolyte and provided a perfect host for encapsulating sulfur.

Fig. 2e, f, k, l and Fig. S6c-d shows TEM images of SRAC/S, OCNA/S and NS-OCNA/S. Fig. S6c,d show that the rod-like carbon material was coated by a thick, nonuniform sulfur layer. As shown, there were many sulfur particles in the pores of the OCNA, but these pores were not filled with sulfur (Fig. 2e) because the dense carbon walls and carbon partitions between the adjacent macropores prevented the penetration of sulfur particles. There were a few sulfur particles embedded in the dense carbon walls (Fig. 2f). As shown in Fig. 2k, the irregular pores in the carbon have entirely disappeared and homogeneous carbon/sulfur composites (NS-OCNA/S) have been formed in their stead due to the facile infiltration of sulfur nanoparticles into the porous carbon walls and the destruction of the carbon partitions. A number of sulfur nanoparticles were uniformly distributed in the carbon hosts (Fig. 2l). The elemental mappings (Fig. 2m-n) of the OCNA/S and NS-OCNA/S composites performed using HAADF-STEM confirmed the elemental distribution. The sulfur nanoparticles can be distinctly distinguished on the STEM image (Fig. 2m). The sulfur and carbon regions exhibited the same rod-like shape, but the rod-like diameter of the sulfur deposits was larger, indicating there was a layer of sulfur that wrapped around the surface of carbon. No conspicuous sulfur nanoparticles can be seen on the surface of the uniform carbon nanoarrays (Fig. 2n). The sulfur, nitrogen and carbon entirely overlapped in the elemental mapping images, suggesting the successful nitrogen doping and well-distributed sulfur loading. It is difficult to ascertain the level of sulfur doping from the elemental mapping, because of the high sulfur content of in the NS-OCNA/S composites.

Fig. 3a describes the X-ray diffraction patterns of the SRAC/S, OCNA/S, NS-OCNA/S and sublimed sulfur. The XRD patterns of SRAC, OCNA and N-OCNA (Fig. S7a) demonstrate their amorphous structure, but it appeared that the N-OCNA contained some degree of crystallinity, which may have been responsible for its better electrical conductivity. Following sulfur loading, the OCNA/S and NS-OCNA/S exhibited the typical features of amorphous carbon without the sharp diffraction peaks of bulk crystalline sulfur, suggesting that the loaded sulfur was well dispersed in the pores of the OCNA and N-OCNA. However, the SRAC/S 'exhibited the crystalline sulfur peaks although they were of exceedingly weak intensity, suggesting that the sulfur successfully covered the SRAC samples [49,50].

The Raman spectra of SRAC/S, OCNA/S, N-OCNA/S and sublimed sulfur are shown in Fig. 3b. The characteristic peaks for sulfur are located at around 157, 221 and 480 cm^{-1}. These peaks were evident in the SRAC/S spectrum even though the peak intensities were much weaker, but Raman peaks for sulfur were not present in the OCNA/S and N-OCNA/S Raman spectra. Moreover, only the OCNA/S and NS-OCNA/S displayed the well-known D-band (1343 cm^{-1}) and G-band (1584 cm^{-1}), which are typical of a disordered carbon and graphitic structure. This was a validation for the good electrical conductivity [51]. In particular, a Raman peak at about 640 cm^{-1} was clearly distinguishable only in the Raman spectrum of the NS-OCNA/S, which was attributed to the C—S bond [52]. This was an indication that sulfur doping had been achieved in this material during the sulfur loading. This also confirmed that nitrogen/sulfur co-doping was successfully achieved through the nitrogen doping and sulfur loading processes. The Raman spectra of SRAC, OCNA and N-OCNA (Fig. S7b) before sulfur loading indicated that the materials had a typical disordered carbon and crystalline graphite structure as evidenced by the well-known D-band (1340 cm^{-1}) and G-band (1580 cm^{-1}). This result provides additional evidence for the high distribution of elemental sulfur in the OCNA/S and NS-OCNA/S composites, with sulfur particles on the SRAC surface.

The pore structure characteristics of the composites before and after sulfur loading are shown in Fig. 3c, d. All the samples exhibited type-IV isotherms with a mesoporous hysteresis loop, indicating the abundant presence of mesopores [53]. Compared to SRAC, OCNA and N-OCNA, the isotherms for the SRAC/S, OCNA/S and NS-OCNA/S materials exhibited deliver a drastic decrease in N_2 adsorption capacity (Fig. 3c), demonstrating the cavities and pores of these materials were generally occupied with sulfur particles. It was noticed that the main pore size distribution fell in the range of 2–30 nm, which provided further evidence of the presence of a mesoporous structure (Fig. 3d). Porosity data for these samples are summarized in Table S2. The SRAC and OCNA materials exhibited specific surface areas of 835 and 1286 $m^2\,g^{-1}$, with the pore volumes of 1.0152 and 1.1103 $cm^3\,g^{-1}$. Therefore, it was concluded that the addition of formaldehyde was not only favorable to the formation of the ordered carbon nanoarrays and pore structures, but was also conducive to an increase in the specific surface areas and pore volume of the products. Furthermore, the S_{BET} and pore volumes of the N-OCNA was abruptly increased to 1625 $m^2\,g^{-1}$ and 1.1676 $cm^3\,g^{-1}$, but the average pore diameter was smaller than OCNA, which was attributed to the change and regulation of the carbon texture and pore structure as a result of nitrogen doping and re-activation by water vapor [54]. As expected, the S_{BET} and pore volume of SRAC/S, OCNA/S and NS-OCNA/S distinctly decreased after loading sulfur, demonstrating that sulfur had infiltrated into the carbon pores. The amount of sulfur in the three composites was determined by thermogravimetric analysis the results are shown in Fig. 3e. The mass losses of the three composites in the temperature range between 180 and 450 °C was attributed to the evaporation of sulfur. Using these data, the sulfur
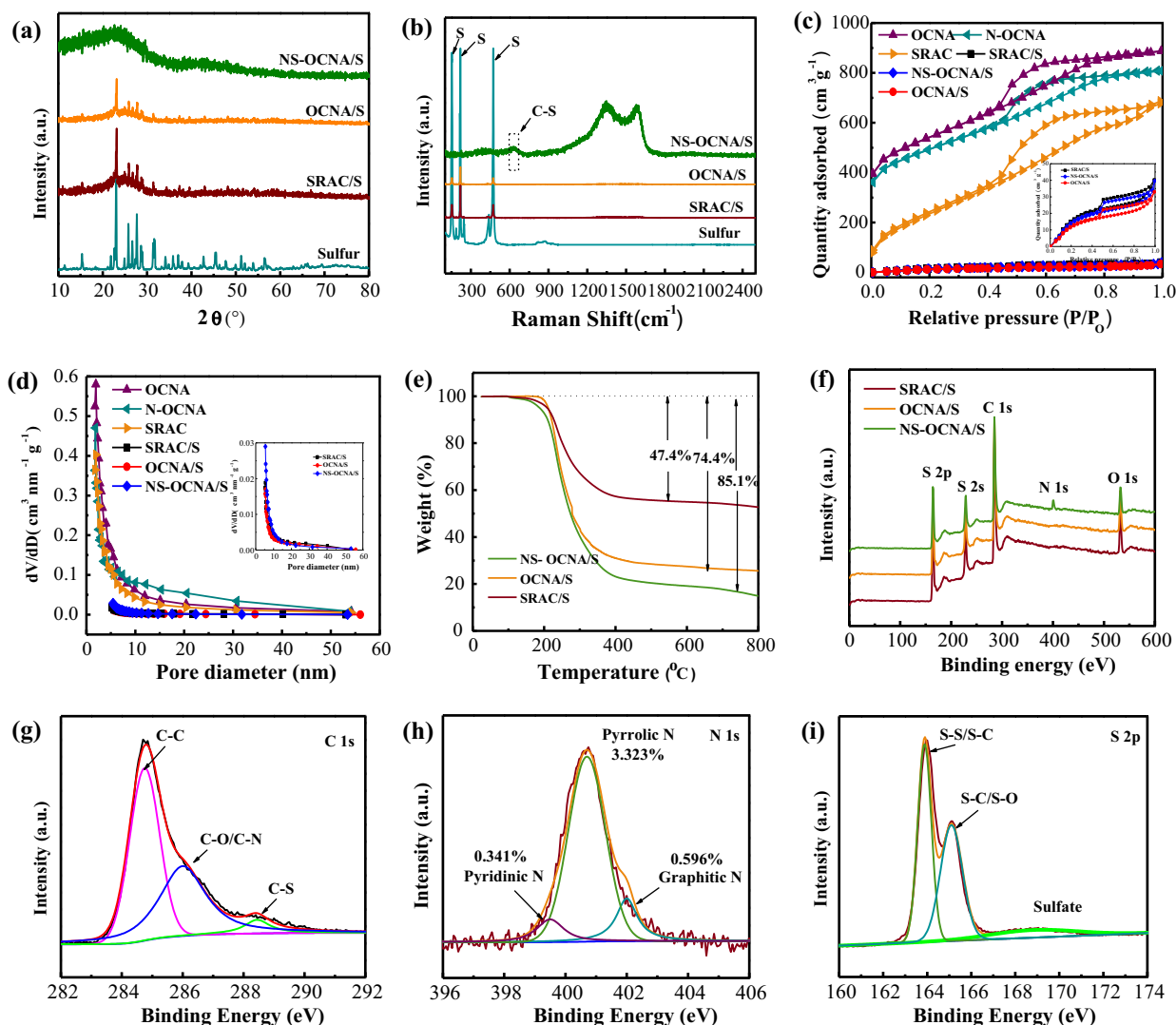
Fig. 3. (a) XRD patterns, (b) Raman spectra of SRAC/S, OCNA/S and NS-OCNA/S and pure sulfur; (c) N₂ adsorption/desorption isotherm; (d) Pore size distributions for SRAC, OCNA, N-OCNA, SRAC/S, OCNA/S and NS-OCNA/S; (e) TGA curves of SRAC/S, OCNA/S and NS-OCNA/S, (f) XPS spectra of SRAC/S, OCNA/S and NS-OCNA/S; High-resolution spectrum of (g) C 1s, (h) N 1s and (i) S 2p for NS-OCNA/S.(j) visual test of the Li₂S₆/DOL-DME solution with different samples.

content of the SRAC/S, OCNA/S and NS-OCNA/S were calculated to be 47.4, 74.4 and 85.1 wt%. Notably, the SRAC/S exhibited the lowest sulfur content because its porosity was lower than the OCNA/S and NS-OCNA/S. In addition, the NS-OCNA/S revealed a lower evaporation rate and higher sulfur loading capacity than OCNA/S, which was an indication of the strong adsorption and obstruction effect of the sulfur after the nitrogen/sulfur co-doping. This was due to the intimate interactions between C, N atoms and S atoms.

The chemical compositions and surface properties of the SRAC, OCNA, N-OCNA and their composites after sulfur loading were determined using via XPS and the results are presented in Fig. 3f–i and Fig. S7c. As shown in the wide-survey XPS spectrum (Fig. 3f), SRAC/S, OCNA/S and NS-OCNA/S exhibited similar peaks at 284.7, 533.2, 164.4 and 228.5 eV, corresponding to C 1s, O 1s, S 2p and S 2s, respectively. The XPS spectra of SRAC, OCNA and N-OCNA also displayed similar peaks at 284.5 and 533.5 eV, corresponding to C 1s and O 1s, respectively (Fig. S7c). Prominently, the N 1s peak at 400.3 eV was only found in the NS-OCNA/S and N-OCNA spectra, showing that reasonable amounts of N had been introduced into the N-OCNA and NS-OCNA/S. In addition, the N 1s spectra of NS-OCNA/S (Fig. 3h) and N-OCNA (Fig. S7e) suggested the presence of nitrogen chemical components, including graphitic

N (0.596%), pyrrolic N (3.323%) and pyridinic N (0.341%), that were identified by the 402.1, 400.7 and 399.3 eV peaks. The presence of these compounds can help to obstruct the dissolution of lithium polysulfides from the carbon due to the strong electronic attraction between the electronegative N atoms and Li⁺. Also, graphitic N can improve the electronic conductivity of the NS-OCNA/S and N-OCNA due to the formation of graphitized fragments. [55] As can be seen from Fig. 3g, the C 1s spectrum of NS-OCNA/S presented three peaks located at 284.7, 286.1 eV and 288.4 eV, which corresponded to the C—C/C≡C, C—O and C—S/C—N groups [56]. For comparison, in the C 1s spectrum of N-OCNA there was no C—S bond (Fig. S7d). This suggested that sulfur was successfully doped into the carbon framework of NS-OCNA/S as further evidenced by the changes in the texture of the carbon and the pore structure caused by nitrogen doping and re-activation by water vapor. Fig. 3i shows the typical S 2p of NS-OCNA/S where two fitted peaks were located at 163.9 eV and 165.1 eV, which was attributed to the S—S/S—C and S—C/S—O groups [57]. The C—S bonds were simultaneously present in the C 1s and S 2p spectra of NS-OCNA/S, which again provided evidence that sulfur had successfully been doped into the carbon framework of NS-OCNA/S, which is to say that nitrogen and sulfur co-doping had been accomplished in the NS-OCNA/S.

The elemental mass percentages as determined from the XPS analysis are summarized in Table S1. As shown, the mass percentage of nitrogen was 4.26% for NS-OCNA/S, and the sulfur content in the SRAC/S, OCNA/S and NS-OCNA/S was 54.67, 77.39 and 83.90%, respectively. This indicated that the NS-OCNA/S effectively immobilized active materials and restricted the dissolution of polysulfides due to its optimum nitrogen/sulfur co-doping.

A four-point probe apparatus was used to determine the electronic conductivities of these prepared SRAC, OCNA, N-OCNA materials and the data are listed in Table S2. Nitrogen doping appeared to increase the electronic conductivity of the material; therefore, the electronic conductivity of the nitrogen doped N-OCNA and NS-OCNA/S was higher than that of the other samples (Table S2). The electronic conductivity of NS-OCNA/S was 0.1254 S cm^{-1} which was higher than that of undoped SRAC (0.0329 S cm^{-1}), illustrating that nitrogen doping was conducive to improving the electrochemical activity of the NS-OCNA/S.

Fig. 4a illustrates the CV curves for the first CV cycles of SRAC/S, OCNA/S and NS-OCNA/S at 0.1 mV s^{-1} in the voltage range of 1.6–3.0 V. In the cathodic scan process, the reduction peak at around 2.28 V corresponded to the reduction of sulfur to higher-order soluble polysulfides (Li$_2$S$_x$, $4 \leq x \leq 8$), while the peak at about 2.04 V was related to the further conversion of high-order soluble polysulfides to insoluble Li$_2$S$_2$ and Li$_2$S. In the subsequent anodic scan process, the broad peak at about 2.43 V was attributed to the oxidization of Li$_2$S$_2$ or Li$_2$S to soluble lithium polysulfides [58]. OCNA/S and NS-OCNA/S displayed more evident reduction peaks at the lower voltage and the two peaks were closer in voltage than SRAC/S, indicating better utilization of the active sulfur and better electrochemical reversibility in the OCNA/S and NS-OCNA/S [59]. Besides, NS-OCNA/S exhibited higher peak current than OCNA/S, demonstrating more energetic redox reaction kinetics. These results illustrate that the formation of an ordered carbon nanoarray structure in the OCNA/S provided more space for sulfur, and the nitrogen/sulfur co-doping of the NS-OCNA/S can further restrict the dissolution of lithium polysulfides in the electrolyte, thereby enhancing the electrochemical performance of the active carbon. The Fig. 4b shows the galvanostatic discharge/charge behaviors of SRAC/S, OCNA/S and NS-OCNA/S at 0.1C (1C = 1675 mA g^{-1}). As can be seen, there were two discharge plateaus at around 2.4 and 2.1 V, and only one broad charge plateau at 2.2–2.4 V in the discharge/charge curves. The initial discharge capacities of SRAC/S, OCNA/S and NS-OCNA/S were 838, 1198 and 1446 mAh g^{-1}, and the charge capacities were 890, 1250 and 1498 mAh g^{-1}. The corresponding coulombic efficiencies were respectively 94.1%, 95.8% and 96.5%. NS-OCNA/S delivered the highest capacity and coulombic efficiency, showing that it provided the best use of sulfur as a result of its more abundant activation points and the stronger chemical bonding of the doped N and S atoms. The Fig. 4c illustrates the cycling performance and coulombic efficiencies of SRAC/S, OCNA/S and NS-OCNA/S at 0.1 C. After 100 cycles, SRAC/S, OCNA/S and NS-OCNA/S achieved reversible capacities of 509, 929 and 1332 mAh g^{-1}, amounting to 60.7%, 77.5% and 92.1% of their initial capacities. This indicated that the ordered porous structure of OCNA/S can load more sulfur that increased the discharge capacity, while the outstanding interactions between the C, N and S atoms in the NS-OCNA/S restrained the dissolution of polysulfides which improved the capacity retention. The synthesized SRAC/S, OCNA/S and NS-OCNA/S were evaluated under various rates as shown in Fig. 4d and e. As shown, the NS-OCNA/S exhibited respectively the highest discharge capacities of 1502, 1446, 1354, 1278 and 1175 mAh g^{-1} when cycled at 0.05, 0.1, 0.2, 0.5 and 1 C. With the current rate backed to 0.1 C after 50 cycles, a high discharge capacity of 1408 mAh g^{-1} was maintained, demonstrating the excellent reversible capacity of NS-OCNA/S. Long-term cycling tests were also conducted for the NS-OCNA/S

electrode at 1C. The initial charge and discharge capacities of the NS-OCNA/S were as high as 1225 and 1175 mAh g^{-1} (Fig. 4f). The discharge capacity of the NS-OCNA/S remained at 932 mAh g^{-1} over 600 cycles, the fade rate was only 0.1% of initial capacity per cycle. In addition, the charge capacities decayed from 914 to 739 mAh g^{-1}, and high capacity retention was 81% over 600 cycles at 2C, indicating outstanding cycling stability. This further demonstrated the remarkably improved electrochemical performance of the NS-OCNA/S, which was attributed to its unique ordered nanoarray structure and good electrical conductivity, but also to the mutual influence of nitrogen/sulfur co-doping, which facilitated rapid electron transfer, that enhanced active carbon utilization and restrained polysulfide dissolution.

Fig. 4g shows the cycling performance of the NS-OCNA/S compared to the most porous carbons used in Li-S batteries within 500 cycles at a rate of 1C [20,60,61]. As shown, the NS-OCNA/S delivered a higher cycling performance. Such a remarkable cycle stability and capability of NS-OCNA/S was owing to the combined effects of the ordered nanoarray structure and appropriate nitrogen/sulfur co-doping of the carbon.

The areal capacity at 0.5 C is plotted versus the cycle number in Fig. 4h. For the different density of NS-OCNA/S electrodes, the initial capacity achieved 3.3, 4.1, and 5.1 mAh cm^{-2}, that corresponded to a remarkable capacity of 1278, 924, and 746 mAh g^{-1} at 2.4, 4.5 and 6.7 mg cm^{-2}, respectively. It can be seen that there was some instability in the areal capacity for the first five cycles, which was attributed to the activating reaction between the electrolyte and active sulfur. Therefore, the NS-OCNA/S electrode at 6.7 mg cm^{-2} displayed an initial increased pattern, because abundant sulfur particles created a step reaction with the electrolyte, and then exhibited a decreased pattern after all the sulfur was involved in the redox reaction. By contrast, with a small sulfur content at 2.4 and 4.5 mg cm^{-2}, the areal capacity was continually reduced because of the dissolution of sulfur, which was removed from the exterior of the carbon. The invertible areal capacities were maintained at high values of 3.0, 3.9 and 4.9 mAh cm^{-2} over 100 cycles, exhibited the superb utilization and retention rate of the active sulfur within NS-OCNA/S.

Electrochemical impedance spectroscopy measurements were conducted before cycling and after 100 cycles at 0.1 C and the analysis of equivalent circuit models are shown in the insets of Fig. 4i and j. As illustrated in Fig. 4i, the Nyquist plots of the carbon/sulfur composites before cycling was composed of a single semicircle in the high frequency that region corresponding to the interface charge-transfer resistance Rct and an inclined line at low frequency represents the Li$^+$ diffusion resistance in the electrodes (W$_c$). After 100 cycles, it was found that all EIS curves showed extra semicircles in the middle frequency that corresponded to the passivation film resistance Rs on the electrodes' surface (Fig. 4j) [62]. It was evident that the resistance of three carbon/sulfur composites had increased after 100 cycles, revealing that the dissolved lithium polysulfides had increased the viscosity of the electrolyte and retarded the Li$^+$ transport (Table S3). It is noteworthy that NS-OCNA/S electrode showed the lowest resistance before and after cycling, suggesting that the NS-OCNA/S had the best electrical conductivity compared to SRAC/S and OCNA/S electrodes, which was consistent its earlier reported electrochemical performance. The corresponding Warburg factors was shown in Fig. 4k and l, and the lithium ion diffusion coefficient (D_{Li^+}) are calculated using the following equation and the results listed in Table S4:

$$D_{Li^+} = \frac{(RT)^2}{2A^2 n^4 F^4 C_{Li^+}^2 \sigma^2} \tag{1}$$

$$Z' = R + \sigma \omega^{-\frac{1}{2}} \tag{2}$$
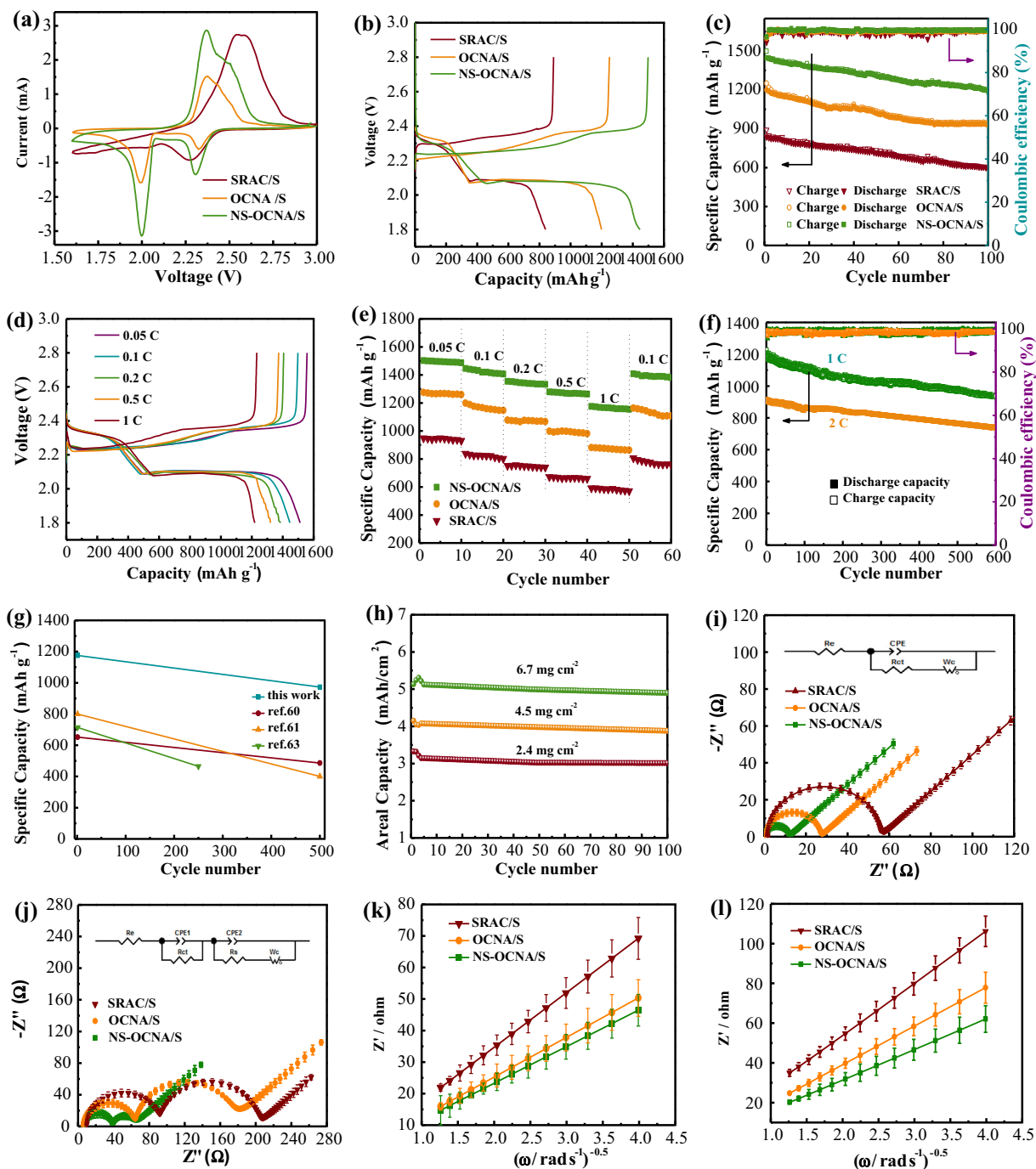
Fig. 4. Cyclic voltammograms of the first cycle (a) SRAC/S, OCNA/S and NS-OCNA/S at a scan rate of 0.1 mV s^{-1} in the voltage range of 1.6–3.0 V; (b) The initial discharge/charge profiles of SRAC/S, OCNA/S and NS-OCNA/S at 0.1 C; (c) Cycling performance and coulombic efficiencies of SRAC/S, OCNA/S and NS-OCNA/S evaluated at a rate of 0.1 C; (d) Galvanostatic charge/discharge profiles at different rates for NS-OCNA/S; (e) The various rate performances for SRAC/S, OCNA/S and NS-OCNA/S; (f) Cycling performance and Coulombic efficiency tested at 1 C and 2 C for NS-OCNA/S; (g) Comparison on cycling performance within 500 cycles at a rate of 1 C; (h) Areal capacity at 0.5 C with different sulfur loading; Nyquist plots (i) before cycling and (j) after 100 cycles (inset: equivalent circuit models) for SRAC/S, OCNA/S and NS-OCNA/S, and the corresponding Warburg factor (k, l), respectively.

where R, T, A, n, F and C are constants, and σ is the slope of the fitted lines, the value of D_{Li^+} is inversely proportional to the value of σ [63]. The straight line in Fig. 4k and l is due to the Warburg diffusion (Ws) in the bulk electrodes, and the lithium ion diffusion velocity of NS-OCNA/S was much faster than that of the other cathodes. This illustrated that an excellent porous structure can provide adequate space for the transmission of lithium ions. In addition, the significant chemical interactions between N, C atoms and S atoms prevent the dissolution of polysulfide thus maintaining decrease the integ-

rity of the electrolyte. Therefore, the NS-OCNA/S appeared to greatly improve the electronic conductivity of the sulfur host.

The OCNA displayed regular macropores like a pod without beans and a small number of inhomogeneous pores in the carbon walls (Fig. 5a). These pores in the carbon walls were too small to benefit sulfur infiltration and loading, and macropores in the middle were so large that they facilitated the dissolution of polysulfides into the electrolyte. After sulfur loading, the regular macropores in the OCNA/S and the surface for carbon rods were
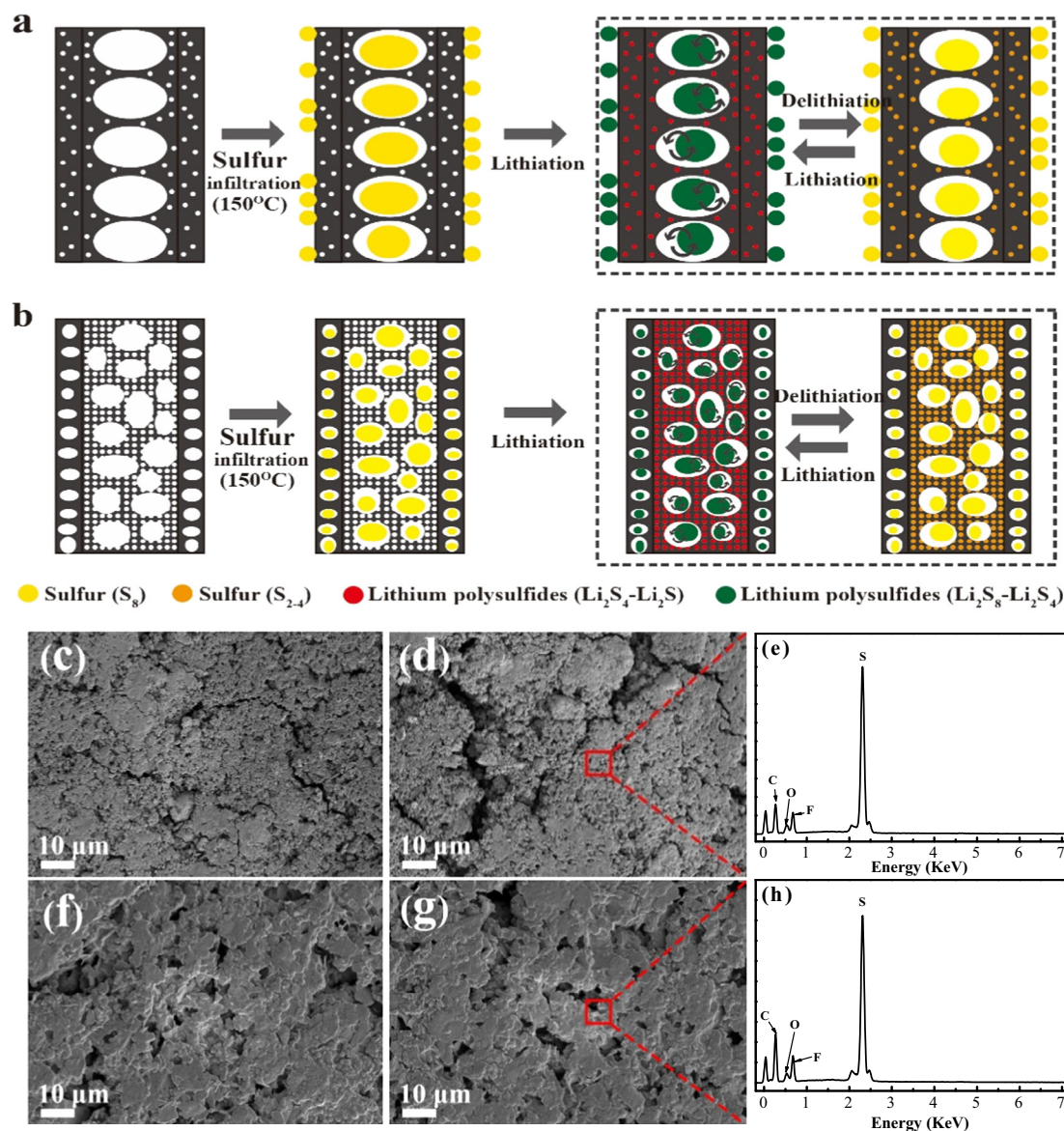
Fig. 5. (a) OCNA/S and (b) NS-OCNA/S schematic illustration of the electrode structures and their electrochemical processes; The SEM images of the OCNA/S (c) and NS-OCNA/S (f) electrodes from fresh cells; The SEM images of the OCNA/S (d) and NS-OCNA/S (g) electrodes after 500 cycles. EDS spectrum of (e) OCNA/S and (h) NS-OCNA/S electrodes.

coated with sulfur particles, but the micropores of OCNA/S in the carbon walls did not contain sulfur. During the charge and discharge processes, a high pore volume is beneficial to the volume expansion of sulfur, but this does not hinder the dissolution of sulfur. In addition, the sulfur particles on the surface of OCNA/S can also easily dissolve into the electrolyte. By contrast, there were suitably sized macropores in the center of the N-OCNA and abundant hierarchical pores in the carbon walls. This was because the pore structure and pore distribution in the N-OCNA resulted from facile KOH activation and was regulated by nitrogen doping and vapor activation in the carbon walls and interior (Fig. 5b). This superior porous structure was favorable for sulfur infiltration and loading, and was also good at restricting the formation of non-conducting sulfur products. In the lithiation process, some S_8 particles were formed in the macropores due to the reduction to soluble polysulfides (Li_2S_x, $4 \leq x \leq 8$), others S_8 formed in these micropores due to the reduction of insoluble short-chain polysulfides (Li_2S_x, $1 \leq x \leq 4$). In the de-lithiation process, the Li_2S_x particles were oxidized at their original positions, and the content of oxidized S_8 was higher than in the OCNA/S. The ordered porous

carbon structure provides a physical limitation to sulfur loading, and N/S co-doping produces strong chemisorption between C, N atoms and S atoms. Therefore, NS-OCNA/S can effectively improve the electrochemical performance of Li-S batteries by increasing the amount of sulfur in the carbon and by restricting the shuttling of polysulfides.

In order to further verify the stability of electrode structures, SEM images were obtained for OCNA/S and NS-OCNA/S from a fresh cell and one that was cycled 500 times. Fig. 5c and f display the OCNA/S and NS-OCNA/S electrodes from the fresh cells, where it can be seen that there are no distinct cracks on the OCNA/S and NS-OCNA/S electrodes. However, major differences were noticed on the OCNA/S electrodes, and the OCNA/S electrode showed obvious and serious developmental fissures after 500 cycles (Fig. 5d). This was a clear indication that the OCNA/S electrode structures had been destroyed by the volume expansion of sulfur and the formation of insoluble lithium polysulfides. Compared to the OCNA/S electrodes, no minute cracks are noticed on the NS-OCNA/S electrodes due to its outstanding restriction for the dissolution of polysulfides (Fig. 5g). EDS data results revealed the elemental

composition of the OCNA/S and NS-OCNA/S electrodes, which contained mainly C, O, F and S, with the F being element is derived from the electrolyte. These results further demonstrate the cycle stability of NS-OCNA/S electrode and are consistent with the previously reported electrochemical test results.

4. Conclusions

On the basis of the methods reported in the previous work [42-47], a new nitrogen/sulfur co-doped, ordered, carbon nanoarray was successfully synthesized from soybean residues using a facile hydrothermal treatment employing ultrasonic atomization and vapor deposition form this work. The resulting NS-OCNA/S composite was meant for use in high-energy-density Li-S batteries and it was found to exhibit an innovative, ordered, carbon-nanoarray. This resulted from the use of formaldehyde as a structure inducing agent using a low-temperature hydrothermal process. The novel carbon material exhibited a high specific surface area, rich porosity, and appropriate N doping. As a positive electrode in a Li-S coin cell battery, the NS-OCNA/S, material exhibited good reversible capacity, cycle stability and rate capability, delivering a high initial discharge capacity of 1446 mAh g^{-1} at 0.1 C. Considering the excellent structure of the nano-carbon materials produced through facile hydrothermal treatment employing ultrasonic atomization and vapor deposition, we believe that the high-performance biomass-derived carbon materials by this way from abundant natural resources for use in Li-S batteries and other systems.

Acknowledgements

Appendix A. Supplementary material

Supplementary data to this article can be found online at https://doi.org/10.1016/j.jcis.2019.07.057.

References

[1] Z. Li, Y.M. Huang, L.X. Yuan, Z.X. Hao, Y.H. Huang, Status and prospects in sulfur-carbon composites as cathode materials for rechargeable lithium-sulfur batteries, Carbon 92 (2015) 41–63.

[2] F. Liu, Q. Xiao, H.B. Wu, F. Sun, X.Y. Liu, F. Li, Z.Y. Le, L. Shen, G. Wang, M. Cai, Y. F. Lu, Regenerative polysulfide-scavenging layers enabling lithium–sulfur batteries with high energy density and prolonged cycling life, ACS Nano 11 (3) (2017) 2697–2705.

[3] X.X. Gu, C.J. Tong, C. Lai, J.X. Qiu, X.X. Huang, W.L. Yang, B. Wen, L.M. Liu, Y.L. Hou, S.Q. Zhang, A porous nitrogen and phosphorous dual doped graphene blocking layer for high performance Li-S batteries, J. Mater. Chem. A 3 (32) (2015) 16670–16678.

[4] T. Maihom, S. Kaewruang, N. Phattharasupakun, N. Phattharasupakun, P. Chiochan, J. Limtrakul, M. Sawangphruk, Lithium bond impact on lithium polysulfide adsorption with functionalized carbon fiber paper interlayers for lithium-sulfur batteries, J. Phys. Chem. C 122 (13) (2018) 7033–7040.

[5] X.Y. Zhou, F. Chen, J. Yang, L.L. Ma, T. Bai, B. Long, Q.C. Liao, C.W. Liu, Dual protection of sulfur by interconnected porous carbon nanorods and graphene sheets for lithium-sulfur batteries, J. Electroanal. Chem. 747 (2015) 59–67.

[6] G.P. Hao, C. Tang, E. Zhang, P.Y. Zhai, J. Yin, W.C. Zhu, Q. Zhang, S. Kaskel, Thermal exfoliation of layered metal-organic frameworks into ultrahydrophilic graphene stacks and their applications in Li-S batteries, Adv. Mater. 29 (37) (2017) 1702829.

[7] W. Ai, W. Zhou, Z. Du, Y. Chen, Z.P. Sun, C. Wu, C.J. Zou, C.G. Li, W. Huang, T. Yu, Nitrogen and phosphorus co-doped hierarchically porous carbon as an efficient sulfur host for Li-S batteries, Energy Storage Mater. 6 (2017) 112–118.

[8] J. Liu, D.G.D. Galpaya, L. Yan, L.J. Yan, M.H. Sun, Z. Lin, C. Yan, C.D. Lianga, S.Q. Zhang, Exploiting a robust biopolymer network binder for an ultrahigh-areal-capacity Li-S battery, Energy Environ. Sci. 10 (3) (2017) 750–755.

[9] M. Yu, Z. Wang, Y. Wang, Y.F. Dong, J.S. Qiu, Freestanding flexible Li$_2$S paper electrode with high mass and capacity loading for high-energy Li-S batteries, Adv. Energy Mater. 7 (17) (2017) 1700018.

[10] J.H. Yan, X.B. Liu, H. Qi, W.Y. Li, Y. Zhou, M. Yao, B.Y. Li, High-performance lithium-sulfur batteries with a cost-effective carbon paper electrode and high sulfur-loading, Chem. Mater. 27 (18) (2015) 6394–6401.

[11] W. Weng, V.G. Pol, K. Amine, Ultrasound assisted design of sulfur/carbon cathodes with partially fluorinated ether electrolytes for highly efficient Li/S batteries, Adv. Mater. 25 (11) (2013) 1608–1615.

[12] Y. Jiang, F. Chen, Y. Gao, Y.Y. Wang, S.S. Wang, Q. Gao, Z. Jiao, B. Zhao, Z.W. Chen, Inhibiting the shuttle effect of Li-S battery with a graphene oxide coating separator: performance improvement and mechanism study, J. Power Sour. 342 (2017) 929–938.

[13] G. Zhou, H. Tian, Y. Jin, X.Y. Tao, B.F. Liu, R.F. Zhang, Z.W. Seh, D. Zhuo, Y.Y. Liu, J. Sun, J. Zhao, C.X. Zu, D.S. Wu, Q.F. Zhan, Catalytic oxidation of Li$_2$S on the surface of metal sulfides for Li-S batteries, Proc. Natl. Acad. Sci. 114 (5) (2017) 840–845.

[14] M. Liu, Q. Li, X. Qin, G.M. Liang, W.J. Han, D. Zhou, Y.B. He, B.H. Li, F.Y. Kang, Suppressing self-discharge and shuttle effect of lithium-sulfur batteries with V$_2$O$_5$-decorated carbon nanofiber interlayer, Small 13 (12) (2017) 1602539.

[15] W. Zhou, C. Wang, Q. Zhang, H.D. Abruña, Y. He, J. Wang, S.X. Mao, X. Xiao, Porous nitrogen-doped carbon derived from silk fibroin protein encapsulating sulfur as a superior cathode material for high-performance lithium–sulfur batteries, Nanoscale 7 (42) (2015) 17791–17797.

[16] N. Li, Z. Weng, Y.R. Wang, F. Li, H.M. Cheng, H.S. Zhou, An aqueous dissolved polysulfide cathode for lithium–sulfur batteries, Energy Environ. Sci. 7 (10) (2014) 3307–3312.

[17] S. Xin, L. Gu, N.H. Zhao, Y.X. Yin, L.J. Zhou, Y.G. Guo, Smaller sulfur molecules promise better lithium-sulfur batteries, JACS 134 (45) (2012) 18510–18513.

[18] M.F. Chen, Q. Lu, S.X. Jiang, C. Huang, X.Y. Wang, B. Wu, K.X. Xiang, Y.T. Wu, MnO$_2$ nanosheets grown on the internal/external surface of N-doped hollow porous carbon nanospheres as the sulfur host of advanced lithium-sulfur batterie, Chem. Eng. J. 335 (2018) 831–842.

[19] F. Ke, Y.Z. Li, C.Y. Zhang, J. Zhu, P.R. Chen, H.X. Ju, Q. Xu, J.F. Zhu, MOG-derived porous FeCo/C nanocomposites as a potential platform for enhanced catalytic activity and lithium-ion batteries performance, J. Coll. Interf. Sci. 522 (2018) 283–290.

[20] Y.Z. Liu, G.R. Li, J. Fu, Z.W. Chen, X.S. Peng, Strings of porous carbon polyhedrons as self-standing cathode host for high-energy-density lithium-sulfur batteries, Angew. Chem. Int. Ed. 56 (22) (2017) 6176–6180.

[21] X. Wu, H.H. Zhang, X.Y. Liu, S.Y. Li, Q.F. Wu, K.J. Huang, Y. Zeng, Z.H. Zhu, Mollusc shell derived 3D porous carbon skeleton for high-performance hybrid electrodes, Electrochim. Acta 294 (2019) 268–275.

[22] Y.P. Gao, Z.B. Zhai, K.J. Huang, Y.Y. Zhang, Energy storage applications of biomass-derived carbon materials: batteries and supercapacitors, New J. Chem. 41 (20) (2017) 11456–11470.

[23] L.L. Xing, G.G. Zhao, K.J. Huang, X. Wu, A yolk–shell V$_2$O$_5$ structure assembled from ultrathin nanosheets and coralline-shaped carbon as advanced electrodes for a high-performance asymmetric supercapacitor, Dalton Trans. 47 (7) (2018) 2256–2265.

[24] L.L. Xing, X. Wu, K.J. Huang, High-performance supercapacitor based on three-dimensional flower-shaped Li$_4$Ti$_5$O$_{12}$-graphene hybrid and pine needles derived honeycomb carbon, J. Coll. Interf. Sci. 529 (2018) 171–179.

[25] L.F. Chen, X.D. Zhang, H.W. Liang, M.G. Kong, Q.F. Guan, P. Chen, Z.Y. Wu, S.H. Yu, Synthesis of nitrogen-doped porous carbon nanofibers as an efficient electrode material for supercapacitors, ACS Nano 6 (8) (2012) 7092–7102.

[26] J. Zhang, J.Y. Xiang, Z.M. Dong, Y. Liu, Y.S. Wu, C.M. Xu, G.H. Du, Biomass derived activated carbon with 3D connected architecture for rechargeable lithium-sulfur batteries, Electrochim. Acta 116 (2014) 146–151.

[27] S.R. Zhao, C.M. Li, W.K. Wang, H. Zhang, M.Y. Gao, X. Xiong, A.B. Wang, K.Q. Yuan, Y.Q. Huang, F. Wang, A novel porous nanocomposite of sulfur/carbon obtained from fish scales for lithium-sulfur batteries, J. Mater. Chem. A 1 (10) (2013) 3334–3339.

[28] X.X. Gu, Y.Z. Wang, C. Lai, J.X. Qiu, S. Li, Y.L. Hou, W. Martens, N. Mahmood, S.Q. Zhang, Microporous bamboo biochar for lithium-sulfur batteries, Nano Res. 8 (1) (2015) 129–139.

[29] J.X. Guo, J. Zhang, F. Jiang, S.H. Zhao, Q.M. Su, G.H. Du, Microporous carbon nanosheets derived from corncobs for lithium-sulfur batteries, Electrochim. Acta 176 (2015) 853–860.

[30] X.X. Gu, C.J. Tong, S. Rehman, L.M. Liu, Y.L. Hou, S.Q. Zhang, Multifunctional nitrogen-doped loofah sponge carbon blocking layer for high-performance rechargeable lithium batteries, ACS Appl. Mater. Interf. 8 (25) (2016) 15991–16001.

[31] J. Yang, F. Chen, C. Li, T. Bai, B. Long, X.Y. Zhou, A free-standing sulfur-doped microporous carbon interlayer derived from luffa sponge for high performance lithium–sulfur batteries, J. Mater. Chem. A 4 (37) (2016) 14324–14333.

[32] S.H. Chung, A. Manthiram, Carbonized eggshell membrane as a natural polysulfide reservoir for highly reversible Li-S batteries, Adv. Mater. 26 (9) (2014) 1360–1365.

[33] S.H. Chung, A. Manthiram, A natural carbonized leaf as polysulfide diffusion inhibitor for high-performance lithium-sulfur battery cells, ChemSusChem 7 (6) (2014) 1655–1661.

[34] M.F. Chen, S.X. Jiang, S.Y. Cai, X.Y. Wang, K.X. Xiang, Z.Y. Ma, P. Song, Adrian C. Fisher, Hierarchical porous carbon modified with ionic surfactants as efficient sulfur hosts for the high-performance lithium-sulfur batteries, Chem. Eng. J. 313 (2017) 404–414.

[35] Z.H. Chen, X.L. Du, J.B. He, F. Li, Y. Wang, Y.L. Li, B. Li, S. Xin, Porous coconut shell carbon offering high retention and deep lithiation of sulfur for lithium-sulfur batteries, ACS Appl. Mater. Interf. 9 (39) (2017) 33855–33862.

[36] M.S. Park, B.O. Jeong, T.J. Kim, S. Kim, K.Y. Kim, J.S. Yu, Y. Jung, Y.J. Kim, Disordered mesoporous carbon as polysulfide reservoir for improved cyclic performance of lithium–sulfur batteries, Carbon 68 (2014) 265–272.

[37] L.L. Xing, K.J. Huang, S.X. Cao, H. Pang, Chestnut shell-like $Li_4Ti_5O_{12}$ hollow spheres for high-performance aqueous asymmetric supercapacitors, Chem. Eng. J. 332 (2018) 253–259.

[38] M.F. Chen, S.X. Jiang, C. Huang, X.Y. Wang, S.Y. Cai, K.X. Xiang, Y.P. Zhang, J.X. Xue, Honeycomb-like nitrogen and sulfur dual-doped hierarchical porous biomass-derived carbon for lithium-sulfur batteries, ChemSusChem 10 (8) (2017) 1803–1812.

[39] J.X. Song, T. Xu, M.L. Gordin, P.Y. Zhu, D.P. Lv, Y.B. Jiang, Y.S. Chen, Y.H. Duan, D. H. Wang, Nitrogen-doped mesoporous carbon promoted chemical adsorption of sulfur and fabrication of high-areal-capacity sulfur cathode with exceptional cycling stability for lithium-sulfur batteries, Adv. Funct. Mater. 24 (9) (2014) 1243–1250.

[40] C. Wang, K. Su, W. Wan, H. Guo, H.H. Zhou, J.T. Chen, X.X. Zhang, Y.H. Huang, High sulfur loading composite wrapped by 3D nitrogen-doped graphene as a cathode material for lithium-sulfur batteries, J. Mater. Chem. A 2 (14) (2014) 5018–5023.

[41] X. Song, S.Q. Wang, Y. Bao, G.X. Liu, W.P. Sun, L.X. Ding, H.K. Liu, H.H. Wang, A high strength, free-standing cathode constructed by regulating graphitization and pore structure in nitrogen-doped carbon nanofibers for flexible lithium-sulfur battery, J. Mater. Chem. A 5 (15) (2017) 6832–6839.

[42] H.J. Denisa, M. Seredych, G.Q. Lu, T.J. Bandosz, Combined effect of nitrogen-and oxygen-containing functional groups of microporous activated carbon on its electrochemical performance in supercapacitors, Adv. Funct. Mater. 19 (3) (2009) 438–447.

[43] W. Xing, C. Liu, Z.Y. Zhou, L. Zhang, J. Zhou, S.P. Zhuo, Z.F. Yan, H. Gao, G.Q. Wang, S.Z. Qian, Superior CO_2 uptake of N-doped activated carbon through hydrogen-bonding interaction, Energy Environ. Sci. 5 (6) (2012) 7323–7327.

[44] C.P. Ruan, K.L. Ai, L.H. Lu, Biomass-derived carbon materials for high-performance supercapacitor electrodes, RSC Adv. 4 (58) (2014) 30887–30895.

[45] H.H. Ru, K.X. Xiang, W. Zhou, Y.R. Zhu, X.S. Zhao, H. Chen, Bean-dreg-derived carbon materials used as superior anode material for lithium-ion batteries, Electrochim. Acta 222 (2016) 551–560.

[46] F. Chen, J. Yang, T. Bai, B. Long, X.Y. Zhou, Biomass waste-derived honeycomb-like nitrogen and oxygen dual-doped porous carbon for high performance lithium-sulfur batteries, Electrochim. Acta 192 (2016) 99–109.

[47] Z.B. Lei, Y. Xiao, L.Q. Dang, W.S. You, Fabrication of ultra-large mesoporous carbon with tunable pore size by monodisperse silica particles derived from seed growth process, Micropor. Mesopor. Mater. 96 (1) (2006) 127–134.

[48] L. Shuai, M.T. Amiri, Y.M. Questell-Santiago, F. Heroguel, Y.D. Li, H. Kim, R. Meilan, C. Chapple, J. Ralph, J.S. Luterbacher, Formaldehyde stabilization facilitates lignin monomer production during biomass depolymerization, Science 354 (6310) (2016) 329–333.

[49] X.Q. Yang, D.C. Wu, X.M. Chen, R.W. Fu, Nitrogen-enriched nanocarbons with a 3-D continuous mesopore structure from polyacrylonitrile for supercapacitor application, J. Phys. Chem. C 114 (18) (2010) 8581–8586.

[50] Y.H. Qiu, Z.A. Zhang, X.H. Zhang, G.D. Ren, X.W. Wang, Y.Q. Lai, Y.X. Liu, J. Li, Synthesis of hierarchical porous honeycomb carbon for lithium-sulfur battery cathode with high rate capability and long cycling stability, Electrochim. Acta 137 (2014) 439–446.

[51] C. Lai, X.P. Gao, B. Zhang, T.Y. Yan, Z. Zhou, Synthesis and electrochemical performance of sulfur/highly porous carbon composites, J. Phys. Chem. C 113 (11) (2009) 4712–4716.

[52] D.H. Seo, A.E. Rider, Z.J. Han, S. Kumar, K. Ostrikov, Plasma breakdown and rebuild: same functional vertical graphenes from diverse natural precursors, Adv. Mater. 25 (39) (2013) 5638–5642.

[53] A.T. Ward, Raman spectroscopy of sulfur, sulfur-selenium, and sulfur-arsenic mixtures, J. Phys. Chem. 72 (12) (1968) 4133–4139.

[54] J.P. Zhao, S.F. Pei, W.C. Ren, L.B. Gao, H.M. Cheng, Efficient preparation of large-area graphene oxide sheets for transparent conductive films, ACS Nano 4 (9) (2010) 5245–5252.

[55] F. Wu, J. Li, Y.F. Tian, Y.F. Su, J. Wang, W. Yang, N. Li, S. Chen, L.Y. Bao, 3D coral-like nitrogen-sulfur co-doped carbon-sulfur composite for high performance lithium-sulfur batteries, Sci. Rep. (2015) 5.

[56] C.X. Zu, A. Manthiram, Hydroxylated graphene-sulfur nanocomposites for high-rate lithium-sulfur batteries, Adv. Energy Mater. 3 (8) (2013) 1008–1012.

[57] X.X. Gu, C. Lai, F. Liu, W.L. Yang, Y.L. Hou, S.H. Zhang, A conductive interwoven bamboo carbon fiber membrane for Li-S batteries, J. Mater. Chem. A 3 (18) (2015) 9502–9509.

[58] S.H. Chung, H.A. Manthiram, A natural carbonized leaf as polysulfide diffusion inhibitor for high-performance lithium-sulfur battery cells, ChemSusChem 7 (6) (2014) 1655–1661.

[59] L.Y. Chai, J.X. Wang, H.Y. Wang, L.Y. Zhang, W.T. Yu, L.Q. Mai, Porous carbonized graphene-embedded fungus film as an interlayer for superior Li-S batteries, Nano Energy 17 (2015) 224–232.

[60] X.L. Yu, J.F. Zhao, R.T. Lv, Q.H. Liang, C.Z. Zhan, Y. Bai, Z.H. Huang, W.C. Shen, F. Y. Kang, Facile synthesis of nitrogen-doped carbon nanosheets with hierarchical porosity for high performance supercapacitors and lithium-sulfur batteries, J. Mater. Chem. A 3 (36) (2015) 18400–18405.

[61] C. Luo, S.Z. Niu, G.M. Zhou, W. Lv, B.H. Li, F.Y. Kang, Q.H. Yang, Dual-functional hard template directed one-step formation of a hierarchical porous carbon–carbon nanotube hybrid for lithium-sulfur batteries, Chem. Commun. 52 (82) (2016) 12143–12146.

[62] H.M. Kim, J.Y. Hwang, A. Manthiran, Y.K. Sun, High-performance lithium-sulfur batteries with a self-assembled multiwall carbon nanotube interlayer and a robust electrode-electrolyte interface, ACS Appl. Mater. Interf. 8 (1) (2016) 983–987.

[63] P. Ge, S. Li, L. Xu, K. Zou, X. Gao, X. Cao, G. Zou, H. Hou, X. Ji, Hierarchical hollow-microsphere metal-selenide@carbon composites with rational surface engineering for advanced sodium storage, Adv. Energy Mater. 9 (2019) 1803035.